Sustainable Carbon Materials

https://doi.org/10.48130/scm-0026-0020

Original Research

Open Access

Cellulose carbon quantum dots decorated CdS nanocatalyst for enhanced visible-light photocatalytic hydrogen evolution

Zijing Wang[1], Rahil Changotra[1], Guofa Dong[2], Jie Yang[3*] and Quan Sophia He[1*]

Received: 19 March 2026

Revised: 10 April 2026

Accepted: 20 April 2026

Published online: 8 June 2026

Abstract

Efficient photocatalytic hydrogen (H_2) production represents a promising pathway towards sustainable energy generation. Cadmium sulfide (CdS)-based semiconductors exhibit excellent potential for visible light-driven photocatalytic H_2 generation; however, their practical application is hindered by photocorrosion, limited absorption in visible light, and a high recombination rate of photogenerated charge carriers. In this study, cellulose-derived carbon quantum dots (CQDs) were synthesized via a hydrothermal method and subsequently decorated onto CdS nanoparticles. The morphological, structural, and optical properties of the as-prepared composites were systematically characterized by a variety of analytical techniques, confirming the successful anchoring of CQDs onto CdS surfaces. The incorporation of CQDs significantly improved the visible-light absorption, reduced the bandgap, and facilitated more efficient charge separation. Among the synthesized composites, the optimized CQDs/CdS photocatalyst achieved the highest H_2 generation rate of 7,812.5 μmol/g within 5 h, which is approximately twice that of undecorated CdS. This remarkable enhancement is attributed to the synergistic effect of CQDs, which act as both photosensitizers and electron acceptors, thereby suppressing charge recombination and increasing electron availability for proton reduction. Overall, these findings highlight the potential of biomass-derived CQDs as efficient photosensitizers for CdS-based photocatalysts, offering a sustainable route to high-performance photocatalytic H_2 generation.

Keywords: CQDs, CdS, Cellulose, Photocatalysis, Hydrogen generation

Highlights

- Cellulose-derived CQDs were synthesized through a sustainable hydrothermal method.
- CQDs were uniformly anchored onto CdS, enhancing visible-light absorption and charge separation.
- The optimized CQDs/CdS catalyst achieved 7,812.4 μmol/g H_2 in 5 h, nearly twice that of pristine CdS.
- CQDs acted as both photosensitizers and electron acceptors, effectively suppressing charge recombination.
- The work demonstrates a green and efficient strategy for improving CdS-based photocatalytic H_2 production.

* Correspondence: Jie Yang (jie.yang@mju.edu.cn); Quan Sophia He (quan.he@dal.ca)

Full list of author information is available at the end of the article.

https://doi.org/10.48130/scm-0026-0020

Graphical abstract

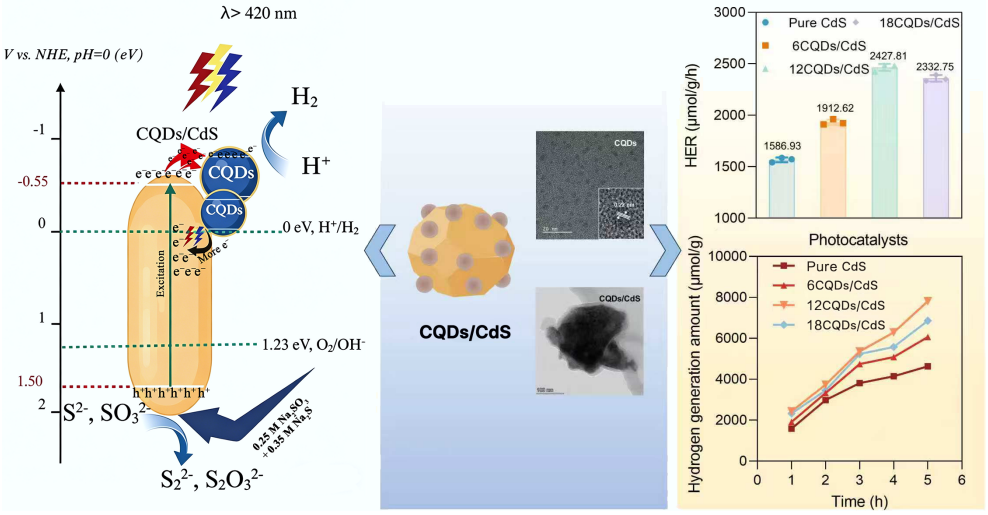

Introduction

Environmental pollution and energy shortages have become significant obstacles to the sustainable development of modern society[1]. In this context, hydrogen (H_2), one of the most promising and important clean renewable resources, has attracted global research interest. Among the various production approaches, photocatalytic water splitting for H_2 evolution provides a highly promising and environmentally friendly way to convert solar energy into green H_2 production[2,3]. Following the pioneering discovery of the excellent photocatalytic performance of TiO_2 in hydrogen evolution reaction (HER)[4], many metal oxides (MOs) such as ZnO[5], and WO_3[6], have been widely explored for photocatalytic H_2 evolution, while they suffer from a wide bandgap due to the high ionicity of the metal-oxygen bonds, allowing them to only absorb UV light, rather than visible light.

To address this limitation, introducing a sulfur vacancy (S vacancy) has been proven to suppress the recombination of charge carriers. Therefore, transition metal sulfides (TMSs) have attracted considerable attention due to their decreased ionicity, which results in higher conductivity and a narrower bandgap, enabling better utilization of visible light. Cadmium sulfide (CdS), a key II–VI group TMS semiconductor, exhibits outstanding performance due to its optimal bandgap energy (E_g= ~2.42 eV) and high absorption coefficient (> 10^4 cm^{-1}). Such properties enable CdS to efficiently absorb visible light up to ~520 nm[7]. Furthermore, CdS possesses a large overpotential (~1.23 eV), which contributes to high reactivity and activity towards HER[8], as it has a suitably negative conduction band and a positive valence band position. Despite these advantages, CdS suffers from severe photo-corrosion, limited absorption in visible light, and a high recombination rate of photogenerated charge carriers[9], all of which limit its photocatalytic performance. To overcome these drawbacks, many modification strategies have been developed to enhance the optical properties and activity of semiconductors, particularly through coupling with other nanomaterials (Supplementary Table S1).

Carbon-based nanomaterials, especially carbon quantum dots (CQDs), have proven to be highly effective photosensitizers that help mitigate photo-corrosion and enhance photocatalytic efficiency[10]. CQDs are quasi-spherical, carbon-based nanomaterials, with diameters typically ranging from 2 to 10 nm, featuring a conjugated π-structure, and enriched functionalized surface groups such as carboxylic acid, hydroxyl, and epoxide moieties. This unique structure promotes excellent absorption in the UV and near-visible regions, high conductivity, hydrophilicity, and efficient electron transfer ability, all of which contribute to enhanced photocatalytic H_2 generation[11]. Unlike many other semiconductor coupling agents, CQDs are notable for their low cost, non-toxicity, and wide availability.

In photocatalytic H_2 generation systems, CQDs act as photosensitizers, extending the light absorption range of the photocatalysts. They also serve as electron acceptors, capturing photoexcited electrons from the host semiconductor and thereby promoting charge separation and increasing the number of electrons available for proton reduction. Numerous studies have demonstrated the beneficial effect of CQDs on H_2 evolution efficiency. For instance, Backes et al.[12] used Cu-doped CQDs to enhance the photocatalytic performance of TiO_2, achieving a H_2 generation rate of 7.2 μmol/g/h. Similarly, Qin & Zeng[13] employed Ag-CQDs onto g-C_3N_4, resulting in a H_2 generation rate of 626.9 μmol/g/h. Smrithi et al.[14] employed beetroot-derived CQDs to modify CdS, achieving a H_2 generation rate of approximately 527.3 μmol/g/h. Collectively, these studies confirm that CQDs significantly enhance photocatalytic H_2 generation efficiency.

Most CQDs reported to date are derived from chemical precursors, typically small organic molecules or synthetic polymers, through synthesis processes, such as acid oxidation, electrochemical synthesis, or pyrolysis. Although these chemical precursors and approaches can synthesize CQDs with desirable optical and electronic properties, they often have several drawbacks, including high cost, harsh reaction conditions, and toxic reagents that pose both environmental and health risks[15]. These limitations have stimulated growing interest in developing greener and more sustainable synthesis routes.

Biomass-derived CQDs have emerged as a sustainable alternative due to their abundance, renewability, and non-toxicity. Compared to chemically derived compounds, biomass-based syntheses generally require milder conditions and generate fewer hazardous by-products, making the process more environmentally friendly and economically viable[16]. Among the various constituents of biomass,

cellulose stands out as a polymer that is structurally uniform and well-defined. Compared with CQDs derived from more heterogeneous biomass sources (e.g., lignin or agricultural residues), cellulose-derived CQDs generally exhibit more uniform particle sizes and consistent morphology[17]. In addition, their hydroxyl-rich structure leads to abundant oxygen-containing functional groups (e.g., C–O and C=O), facilitating stronger interfacial interactions. From an optoelectronic perspective, cellulose-derived CQDs typically show more stable optical properties due to their relatively controlled carbonization process. These features make cellulose an ideal precursor for achieving better control over the structural and optoelectronic properties of CQDs.

Despite extensive efforts in developing CdS-based photocatalysts, most reported strategies rely on cocatalyst loading or complex heterostructure engineering to improve charge separation efficiency. By contrast, the use of biomass-derived CQDs as interfacial modifiers, particularly those derived from structurally well-defined cellulose, has not been sufficiently explored. In this study, cellulose-derived CQDs were synthesized via a hydrothermal process and integrated with CdS nanoparticles to construct a CQDs/CdS composite system. This work focuses on employing cellulose-derived CQDs as sustainable and structurally controllable interfacial modifiers to regulate charge transfer and suppress recombination, without relying on noble metals or complex architectures. The resulting catalysts were comprehensively characterized using various analytical techniques to elucidate their structural, optical, and electronic properties, providing insights into their photocatalytic H_2 generation mechanism. Furthermore, the photocatalytic stability and reusability of CQDs/CdS catalysts were evaluated to assess their practical applicability.

Materials and methods

Materials

Microcrystalline cellulose derived from corn core was purchased from Alfa Aesar Co., Ltd, USA. Cadmium chloride hydrate (99.0%), thiourea (99.0%), sodium sulfide hydrate (99.0%), sodium sulfite (99.0%), sodium sulfate (99.0%), potassium chloride (99.0%), quinine sulfate (99.0%), ethanol, and FTO (fluorine-doped tin oxide) coated glass sheet (50 nm × 50 nm × 2.2 mm, surface resistivity ~7 Ω/sq) were all purchased from Sigma-Aldrich. Microporous nylon filter membrane (47 mm, 0.22 μm pore size) was acquired from GVS North America (USA). A 1 kDa molecular weight cut-off dialysis membrane was supplied by Spectrum Laboratories, Inc. Deionized water (DI water) was achieved from a Millipore UV water purification system (Direct-Q, Millipore, USA). All chemicals and materials used were of analytical grade and used without further purification.

CQDs synthesis

A mixture of 0.4 g cellulose powder and 40 mL of DI water was loaded into a 50 mL Teflon-lined stainless-steel autoclave. After thorough stirring for 5 min to ensure uniform dispersion, the reactor was heated in an oven to 200 °C and maintained at that temperature for 12 h. Subsequently, the reactor was allowed to cool down naturally to room temperature. The resulting suspension was then centrifuged and filtered through a 0.22 μm filter membrane to remove any insoluble residues. The filtrate obtained was further purified using a dialysis membrane for five days to remove remaining impurities and salts. The obtained CQD solutions were stored at 4 °C until further use.

CdS synthesis

A 0.13 M solution of cadmium chloride hydrate was prepared by dissolving it in 70 mL of DI water. To this solution, 0.73 M of thiourea was added, followed by continuous stirring for 2 h to ensure proper mixing. Subsequently, the obtained solution was transferred into a 250 mL Teflon-lined autoclave and subjected to hydrothermal treatment at 180 °C for 24 h. After the reaction, the orange precipitate was collected and washed twice with DI water and once with ethanol, and was subsequently dried in an oven at 80 °C for 12 h. The final product was labelled as pure CdS.

CQDs/CdS synthesis

The CQDs/CdS composites were synthesized using a hydrothermal method. Specifically, 0.15 g of as-prepared CdS and varying volumes of CQD solutions at 0, 6, 12, and 18 mL were dispersed in 40 mL of ethanol. After being stirred for 2 h, the suspension was transferred into a 50 mL Teflon-lined autoclave and heated at 120 °C for 2 h. After cooling to room temperature, the resulting CQDs/CdS composites were collected by filtration, dried at 80 °C for 12 h, and labelled as pure CdS, 6CQDs/CdS, 12CQDs/CdS, and 18CQDs/CdS, respectively.

Characterization

The surface morphology and microcrystalline structure of the synthesized photocatalysts were examined using a field-emission scanning electron microscope equipped with an energy-dispersive X-ray spectroscopy detector (FE-SEM/EDS, JEOL JSM-6510LV, Japan) and a high-resolution transmission electron microscope (HR-TEM, JEOL JEM-F200, Japan). The elemental composition and chemical bonding states of as-prepared nanocomposites were analyzed by AlKa X-ray photoelectron spectroscopy (hv = 1,486 eV) (XPS, ESCA+, Omicron Nanotechnology, Oxford Instruments, Germany), under ultra-high vacuum conditions. All XPS data were analyzed using CasaXPS software. The surface functional groups were identified using a Fourier Transform Infrared Spectroscopy (FTIR, PerkinElmer, Spectrum 2, USA), in the range of 4,000 and 500 cm^{-1} at the best resolution of 0.5 cm^{-1}. The internal structure and crystallinity of the as-prepared photocatalysts were determined by X-Ray Diffraction (XRD, Philips PW 30590/60 XPERT-PRO diffractometer, Austria) with Cu Kα radiation (λ = 0.154 nm, 45 kV, and 40 mA). The optical absorption in the range of 200–800 nm and the corresponding bandgap energy of the synthesized photocatalysts were determined via a UV-vis DRS spectrophotometer (UV-vis DRS, T8DCS, Persee, China), with $BaSO_4$ serving as the reference standard. The photoluminescence (PL) and time-resolved PL decay spectra of the solid photocatalysts were recorded using a fluorescence spectrometer (PL, PerkinElmer LS55, USA) under 370 nm excitation wavelength. The PL spectra of CQDs in liquid form were obtained by fluorescence spectroscope (TECAN NC-27560, USA) with excitation wavelengths ranging from 310 to 400 nm. The optical absorption behavior of the synthesized CQDs was examined using a UV-vis spectrophotometer (HACH DR6000, Germany).

Photoluminescence quantum yield

Photoluminescence quantum yield of CQDs was determined in relation to quinine sulfate dissolved in 0.1 M H_2SO_4 (Φ_R = 0.546) as a reference[18]. The photoluminescence quantum yield of cellulose CQDs was calculated using the following equation:

$$\Phi_s = \Phi_R \times \frac{I_s}{I_R} \times \frac{A_R}{A_s} \quad (1)$$

where, Φ_s, and Φ_R represent the photoluminescence quantum yield of the sample, and reference, respectively; I_s and I_R respectively denote

https://doi.org/10.48130/scm-0026-0020

the integrated emission intensity obtained at emission wavelength (λ_{ex} = 350 nm); A_R and A_s are the absorbance measured at the same excitation wavelength.

Photoelectrochemical study

The photoelectrochemical properties of the synthesized CQDs/CdS nanocomposites were evaluated using a 1010E Potentiostat (Gamry Instruments, USA) in a three-electrode configuration under illumination from a solar simulator (300 W Xe lamp, Newport-MKS Instruments, USA). A platinum mesh served as the counter electrode, while a saturated Ag/AgCl electrode (1 M KCl) was used as the reference electrode. The working electrode was prepared on an FTO sheet that was first ultrasonically cleaned in ethanol for 30 min and then air-dried. Subsequently, 20 mg of the as-prepared catalyst was dispersed in 200 μL of ethanol and sonicated for 15 min to form a homogeneous slurry. This suspension was evenly spread onto the cleaned FTO sheet over an area of 1 cm^2. After air drying for 40 min, the electrodes were further dried in a muffle furnace at 120 °C for 2 h with a heating rate of 5 °C/min, followed by natural cooling to room temperature.

Photocatalytic H_2 generation experiments

Photocatalytic H_2 generation experiments were carried out in a 280 mL conical flask that served as the reactor and was sealed with a rubber stopper. In each experiment, 20 mg of the catalyst was dispersed in 100 mL of an aqueous solution containing 0.25 M Na_2SO_3 and 0.35 M Na_2S, which acted as sacrificial agents. Prior to irradiation, the reactor was purged with nitrogen gas for 1 h under continuous stirring to remove dissolved oxygen. The sealed reactor was then irradiated with a 300 W Xe lamp equipped with a UV-cutoff filter, with a distance of 20 cm between the light source and the reactor, while stirring was continued throughout the reaction. The produced H_2 was quantified using a micro gas chromatography (Micro-GC/TCD, PerkinElmer-Clarus 590, USA) fitted with a molecular sieve column (1m, 5X A) and a thermal conductivity detector. Gas samples (5 mL) were withdrawn from the reactor using a precision gas-tight syringe (Supeico-Pressure-LoK® Series A-2, USA) for analysis.

Results and discussion

Morphology of CQDs and CQDs/CdS nanoparticles

The surface morphology and microstructure of the synthesized materials were examined using HRTEM (Fig. 1f, g) and SEM-EDX (Fig. 1b–d). The SEM-EDX and HRTEM-SAED analyses confirm that the CQDs are successfully anchored on the CdS surface without significantly changing the morphology or size of CdS.

Details, as shown in Fig. 1b, the CdS nanoparticles exhibit a microspherical morphology composed of densely packed, irregularly faceted nanoparticles ranging in size from 190 to 600 nm. The introduction of CQDs does not significantly alter the overall morphology or size of CdS. However, the surface of the CdS nanoparticles becomes relatively smooth after CQD modification (Fig. 1c). This observation suggests a possible surface passivation effect of CQDs on CdS nanoparticles. Figure 1d exhibits the EDX mapping of 12CQDs/CdS, confirming the presence of the Cd and S elements originating from CdS, along with C, N, and O elements from CQDs. In Supplementary Fig. S1, the EDS spectra further determine the weight% and atomic% of each element. The C element is 1.70 weight% and 9.37 atomic%, suggesting the low loading of CQDs.

Furthermore, HRTEM analysis was conducted to gain deeper insight into the internal crystalline structure of the samples. The HRTEM image of the CQDs (Fig. 1e) shows numerous homogeneously dispersed spherical nanoparticles without noticeable aggregation. The CQDs exhibit an average particle size of 3.5 nm and present clear lattice fringes with an interplanar spacing of 0.22 nm, corresponding to the (100) plane of graphitic carbon[19]. In the case of pure CdS (Fig. 1f), distinct lattice fringes with a d-spacing of 0.36 nm are observed, which is consistent with the (100) plane of the wurtzite CdS phase. Figure 1g shows the HRTEM images of the CQDs/CdS composites with two distinct lattice fringes, 0.22 and 0.34 nm, which can be attributed to the (100) plane of CQDs and the (002) plane of CdS, respectively. This observation suggests the successful integration of CQDs onto the CdS surface. Furthermore, the SAED pattern of the CQDs/CdS composite (Fig. 1g) displays diffraction rings corresponding to the CQDs (100) plane and the CdS (002) and (112) planes, further verifying the coexistence of both components in the composite.

Crystal structure and functional group analysis

The crystal structure of CdS and CQDs/CdS composites was analyzed using XRD, as illustrated in Fig. 2. The diffraction peaks at 24.8° (100), 26.8° (002), 28.3° (101), 36.7° (102), and 43.8° (110) correspond to the major characteristic reflections of hexagonal wurtzite CdS. No additional diffraction peaks are detected in the CQDs/CdS composites, indicating that the incorporation of CQDs has minimal impact on the overall crystalline phase of CdS. This indicates that the CQDs are likely to anchor on the surface of CdS rather than be integrated into its lattice, which minimizes structural defects. These findings are consistent with previous studies reported by Chai et al.[20] and Gogoi et al.[21]. Figure 2 shows that the primary diffraction peaks of CQDs/CdS are slightly shifted towards lower 2θ values when compared to pure CdS. This shift implies a slight lattice expansion and an increase in interplanar spacing[22]. This shift can be attributed to interfacial interactions between CQDs and CdS, which may induce local lattice distortion or strain, rather than lattice incorporation of CQDs[21].

Figure 2c presents the FTIR spectra of pure cellulose and cellulose-derived CQDs. The characteristic broad absorption observed around 3,400 cm^{-1} corresponds to hydroxyl (–OH) group stretching vibrations, while the band near 2,120 cm^{-1} is assigned to C=N stretching vibrations, which are typically associated with nitrogen-containing surface groups formed during the hydrothermal process[23]. The peak at 1,640 cm^{-1} corresponds to the C=C stretching vibrations of aromatic domains within the CQD structure. The cellulose-derived CQDs show enhanced –OH and C=C signals, confirming the formation of conjugated carbon networks and oxygen-containing functional groups. In addition, the absorption near 620 cm^{-1} corresponds to out-of-plane bending of C–H bonds in aromatic rings, further supporting CQD formation[24].

Figure 2d displays that the FTIR spectra of pure CdS and CQDs/CdS composites exhibit similar characteristic absorption bands, indicating that CQD incorporation does not significantly alter the main chemical framework of CdS. The broad band around 3,400 cm^{-1} corresponds to the stretching vibrations of the –OH[25]. The absorption band between 2,899–2,999 cm^{-1} is attributed to C–H stretching vibrations, originating from the carbonaceous CQDs components. A weaker band near 1,605 cm^{-1} can be assigned to C=C/C=O stretching in aromatic or carbonyl groups, suggesting the presence of surface functional moieties contributed by CQDs. Additionally, distinct absorption peaks at 1,130 and 660 cm^{-1} are associated with C–O–C stretching of ether linkages and C–OH stretching of alcohol groups, respectively[22,26]. These signals highlight the hydrophilic character of CQDs and confirm their successful integration with CdS.

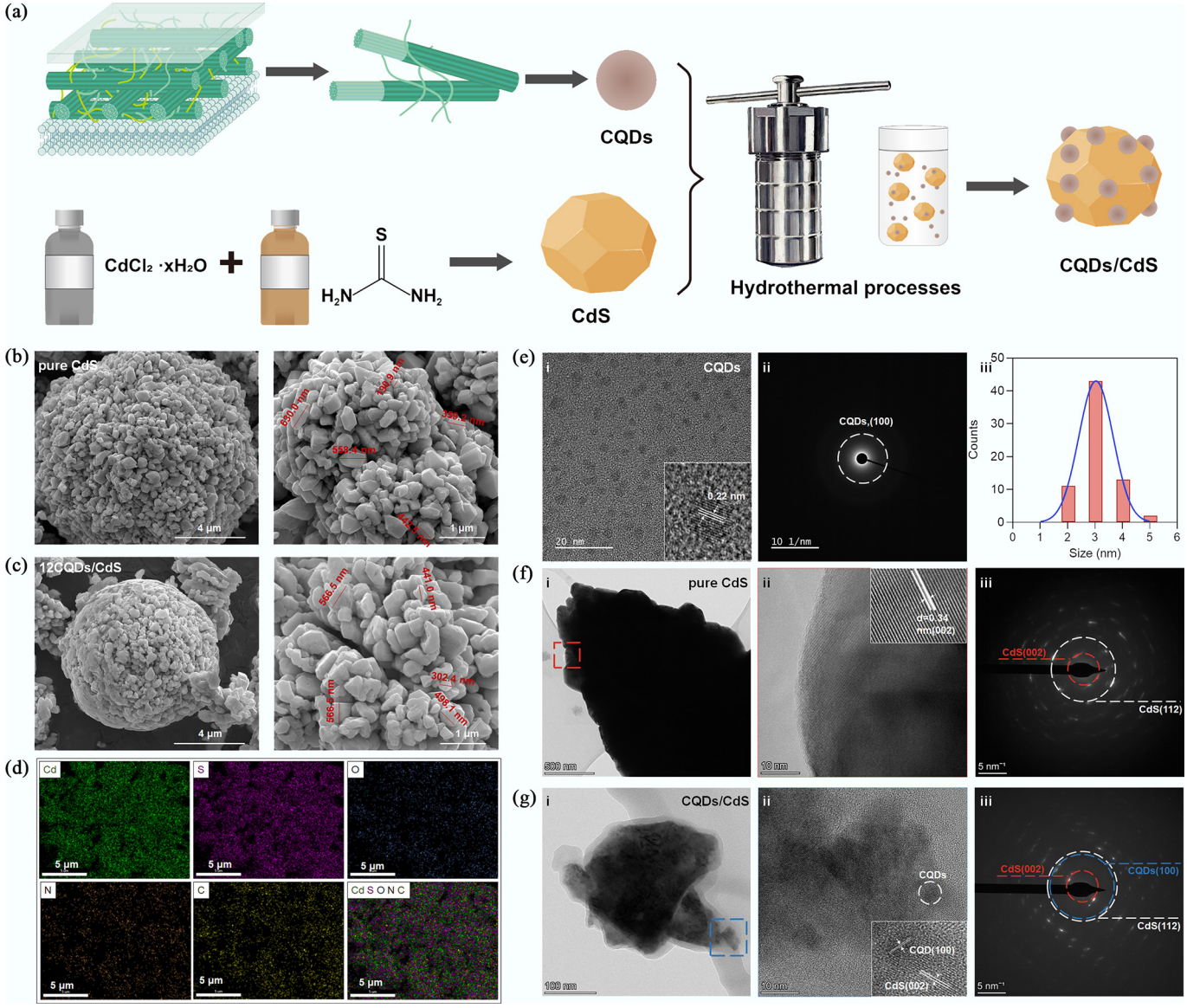

Fig. 1 (**a**) The schematic illustration of fabrication process of CQDs/CdS; SEM images of (**b**) pure CdS, and (**c**) 12CQDs/CdS; (**d**) EDX mapping of 12CQDs/CdS; (**e**) i. HRTEM, ii. SAED pattern, and iii. particle size distribution of CQDs; (**f**) i & ii. HRTEM, and iii. SAED pattern of pure CdS; (**g**) i & ii. HRTEM, and iii. SAED pattern of CQDs/CdS.

Importantly, the characteristic peaks of CdS remain unchanged after CQD incorporation, suggesting that the crystal lattice and chemical structure of CdS are well preserved. These observations are fully consistent with reports in the literature[11,27] and align well with the XPS results (Fig. 3), confirming the successful incorporation of CQDs into the CdS matrix without structural degradation.

Elemental composition and chemical state analysis

XPS analysis was utilized to examine the chemical bonding and internal interaction between CdS and CQDs. The XPS survey spectrum (Fig. 3a) confirms the presence of Cd, S, and C elements in the 12CQDs/CdS composite. The Cd 3d spectrum (Fig. 3b) displays two characteristic peaks at 405.31 and 412.04 eV, corresponding to Cd $3d_{5/2}$ and Cd $3d_{3/2}$ of Cd^{2+} in CdS, with a spin-orbit splitting energy of 6.83 eV. After CQDs incorporation, the Cd 3d and the spectrum of 12CQDs/CdS become broadened and can be deconvoluted into two sets of spin-orbit doublets. The peaks centered at 406.07 and 412.65 eV are attributed to Cd^{2+} species in a relatively electron-deficient environment (denoted as surface Cd), while those at lower binding energies correspond to Cd^{2+} in the CdS lattice (inner Cd)[28]. Similarly, the high-resolution S 2p spectrum (Fig. 3c) exhibits two peaks at 161.61 and 162.81 eV, which are assigned to S $2p_{3/2}$ and S $2p_{1/2}$, respectively, indicating the presence of S^{2-} in CdS[29]. In contrast, the 12CQDs/CdS sample shows additional components, which can be assigned to surface S species, suggesting that the local chemical environment of sulfur is also modified. Compared with pure CdS, the Cd 3d and S 2p peaks in 12CQDs/CdS exhibit a red shift towards higher binding energies, suggesting a decrease in electron density within the composite[30].

Additionally, the high-resolution C 1s spectrum of 12CQDs/CdS was studied (Fig. 3d), which shows four distinct peaks at 284.78, 286.31, 287.82, and 288.81 eV. These correspond to C–H/C–C

https://doi.org/10.48130/scm-0026-0020

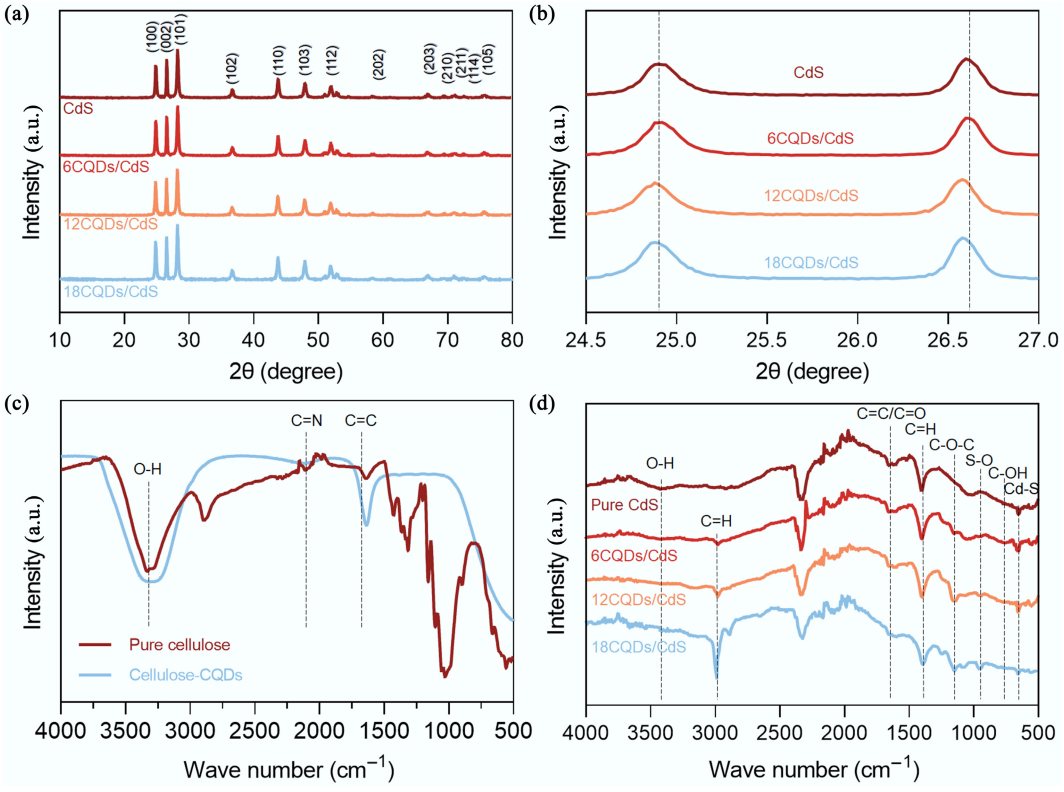

Fig. 2 (**a**) Full range XRD pattern, and (**b**) high-resolution XRD pattern of CQDs/CdS composites; (**c**) FTIR spectrum of pure cellulose and cellulose-derived CQDs, and (**d**) of pure CdS, and CQDs/CdS.

(80.23%), C–OH/C–O–C (11.67%), C=O (3.95%), and O–C=O (4.15%) functional groups, respectively[26]. In contrast, the pure CdS exhibits weak C and O signals (C–C, C–OH, and C=O bonds), which is mainly attributed to minor organic contamination adsorbed during XPS analysis; a phenomenon reported in the literature[27, 31]. In the O 1s spectrum (Fig. 3e), the fitted peaks in the 531.89 and 532.95 eV regions may be attributed to adsorbed water and surface oxygen-containing species. Thus, for the O 1s spectrum of 12CQDs/CdS, more oxygen-containing functional groups from CQDs (e.g., C=O, C–O–C, and surface hydroxyl groups) were induced in CdS, as supported by the C 1s and FTIR results. Notably, compared with pure CdS, both C 1s and O 1s spectra of 12CQDs/CdS show slight shifts towards lower binding energies, indicating an increase in electron density. This behavior suggests interfacial electronic interaction between CdS and CQDs, accompanied by charge redistribution at the interface. Overall, the XPS results imply a possible electron transfer from CdS to CQDs, highlighting the role of CQDs as electron acceptors in the composite system.

Optical characteristics of CdS and CQDs/CdS

The optical properties of the prepared CQDs were characterized by testing their photoluminescence quantum yield, UV-vis spectrometer (Fig. 4a), and PL spectrometer (Fig. 4b). The optical properties of the CQD/CdS were assessed using UV-vis DRS spectrum (Fig. 4c), and Tauc plot (Fig. 4d).

The as-prepared CQDs exhibited a photoluminescence quantum yield of 7.65%. The UV-vis absorption spectrum (Fig. 4a) of the synthesized CQDs exhibits three distinct absorption bands at approximately 210, 268, and 303 nm, which are characteristic of carbon-based nanostructures. The intense peaks around 210 and 268 nm correspond to π–π^* transitions of the conjugated sp^2-hybridized carbon domains (C=C bonds), indicating the presence of graphitic regions within the CQD structure[23]. The shoulder peak observed near 303 nm is associated with n–π^* transitions arising from oxygen-containing functional groups such as C=O or C=OH[32], indicating surface oxidation and functionalization of the CQDs. The PL spectrum of the CQDs (Fig. 4b) reveals an excitation-dependent fluorescence emission behavior. As the excitation wavelength increases from 310 to 410 nm, a noticeable red shift in the emission peak is observed, indicating the presence of multiple emissive sites or energy states of the CQDs[33]. This behavior is commonly attributed to variations in surface defects, particle size distribution, and different functional groups on the CQD surface, which together contribute to their tunable optical properties.

The UV-vis DRS spectra (Fig. 4c) and the corresponding Tauc plots (Fig. 4d) were obtained to examine the light absorption ability and bandgap energies (E_g) of CdS and CQDs/CdS composites. As shown in Fig. 4c, all samples exhibit strong optical absorption across the UV to visible light spectrum (200–600 nm). Compared with pure CDs, the CQDs/CdS composites exhibit a slight red shift in their absorption edges, indicating that the incorporation of CQDs enhances visible-light absorption. This enhancement suggests that CQDs function as effective photosensitizers, thereby broadening the light-harvesting range of the photocatalytic system. The optical band energies (E_g) of CdS and CQDs/CdS were determined using the Kubelka-Munk function:

$$(\alpha h\nu)^{1/2} = A\left(h\nu - E_g\right) \quad (2)$$

where, A, h, α, and ν are proportionality constant, Plank's constant, absorption coefficient, and the frequency of the incident light,

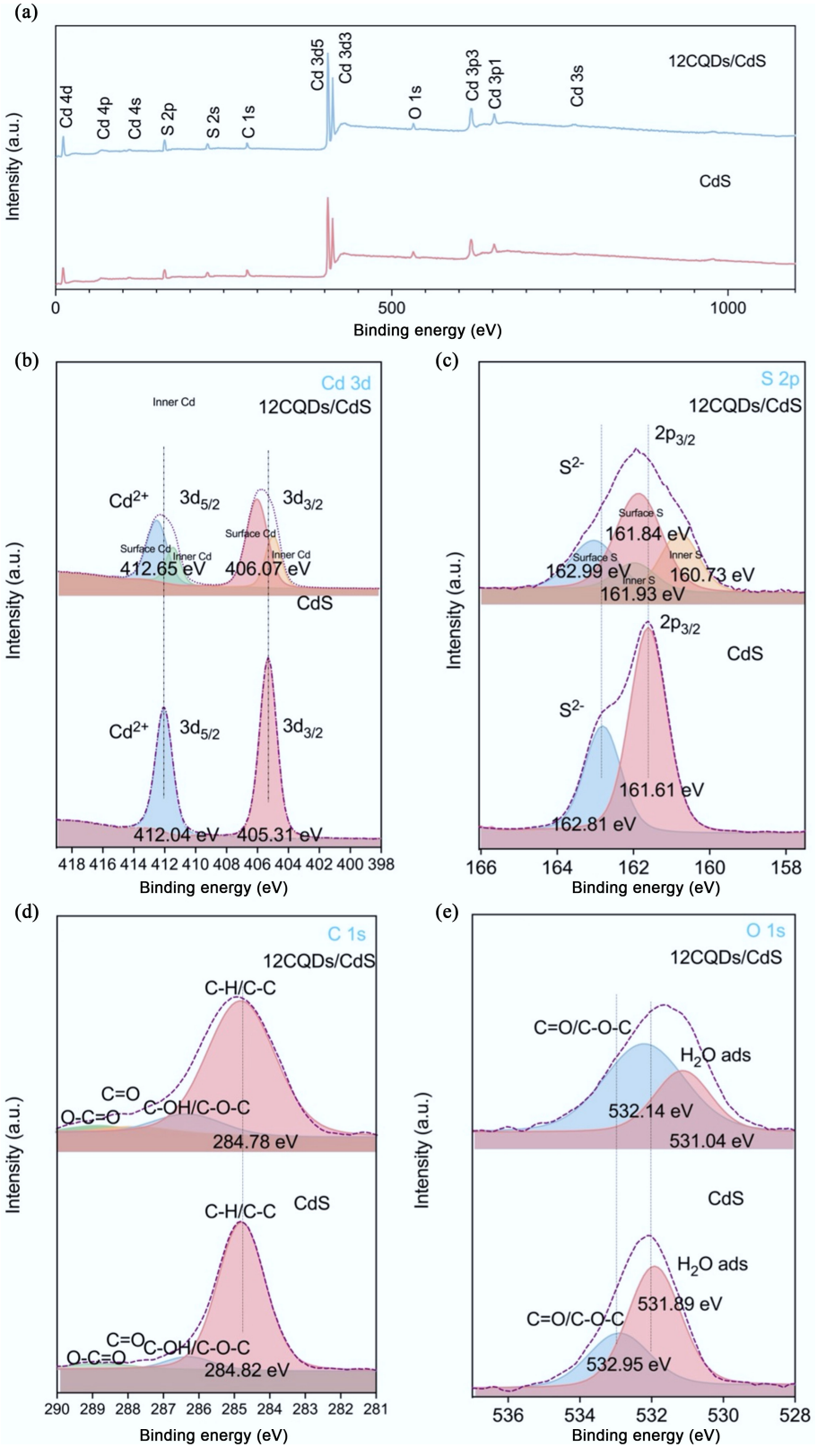

Fig. 3 (**a**) XPS survey spectrum of pure CdS, and 12CQDs/CdS. High-resolution XPS spectrum of (**b**) Cd 3d, (**c**) S 2p, (**d**) C 1s, and (**e**) O 1s.

respectively. The calculated E_g values (Fig. 4d) for pure CdS, 6CQDs/CdS, 12CQDs/CdS, and 18CQDs/CdS are 2.05, 2.03, 2.01, and 2.02 eV, respectively. All CQDs/CdS composites exhibit slightly narrower band gaps compared to pure CdS, suggesting improved visible-light absorption capabilities. Among the photocatalysts, 12CQDs/CdS shows the smallest bandgap, which can be attributed to the strong

https://doi.org/10.48130/scm-0026-0020

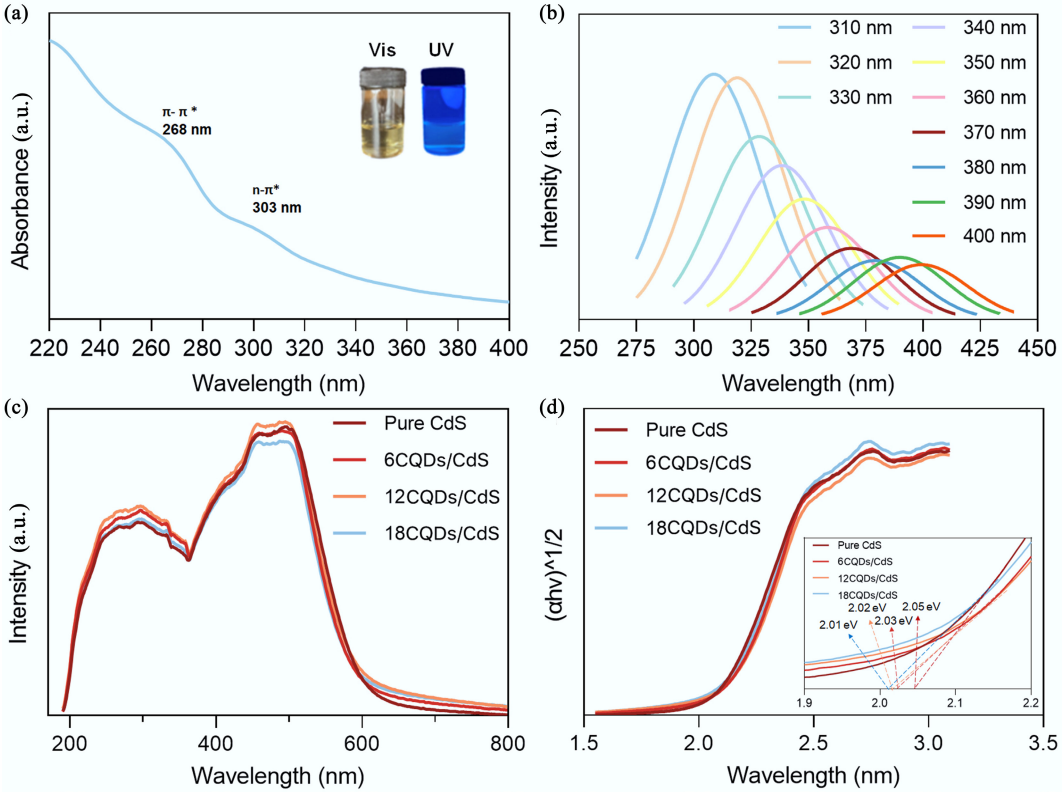

Fig. 4 (**a**) UV-vis spectrum; (**b**) PL spectrum of CQDs at excitation wavelength from 310 to 400 nm; (**c**) UV-vis DRS spectrum, and (**d**) Tauc plot of pure CdS, 6CQDs/CdS, 12CQDs/CdS, and 18CQDs/CdS.

interfacial interaction between CQDs and CdS, and the formation of shallow trap states that facilitate charge transfer[34]. However, when the CQD loading is further increased to 18 mL, a minor increase in bandgap is observed. This can be attributed to excessive CQD coverage, which can block the active sites of CdS or partially hinder light penetration, thereby reducing the efficiency of band structure modulation and photon absorption[35].

Photocatalytic H2 generation performance

To systematically establish the optimal reaction parameters for CdS-based photocatalytic hydrogen evolution, a series of control experiments were first conducted to examine the effects of sacrificial agents, catalyst loading, and light source. The sacrificial agent selectivity of CdS was first evaluated using 0.25 M Na_2SO_3, glucose, and methanol (Fig. 5a). Among these, the combination solution of 0.25 M Na_2SO_3 and 0.35 M Na_2S exhibits the highest H_2 evolution rate of 1,586.9 μmol/g/h, demonstrating its superior hole-scavenging ability. This may be because S^{2-} in Na_2S rapidly captures photogenerated holes, while SO_3^{2-} in Na_2SO_3 converts the formed S^0 into soluble polysulfide species, thereby preventing the deposition of sulfur on the CdS surface and suppressing photo-corrosion[36]. Accordingly, this combination is selected as the optimal sacrificial system for subsequent CdS-based photocatalytic H_2 evolution tests.

The effects of catalyst loading (5 mg/25 mL vs 20 mg/100 mL) (Fig. 5b) and the light source (UV-vis vs vis) were then simply investigated by comparing their H_2 evolution, revealing that 20 mg CdS in 100 mL under only visible light provides more stable and efficient catalytic performance (1,226.8 μmol/g/h). The reason may be attributed to the illuminated area and photocorrosion. The 20 mg CdS sample in 100 mL solution had a larger light-receiving area, which enhanced light absorption and consequently increased H_2 production[37]. CdS is more susceptible to photocorrosion under UV irradiation, which likely contributes to the reduced H_2 evolution performance under UV-vis light. In addition, under high-energy excitation, the sulfur ions are attacked by photogenerated holes and oxidized into elemental sulfur[9]. The XRD spectrum of 12 CQDs/CdS (Supplementary Fig. S2) after reaction also suggests the occurrence of photocorrosion. Therefore, the optimized conditions were determined, including 0.25 M Na_2SO_3 and 0.35 M Na_2S as a sacrificing agent, 20 mg/100 mL as the catalyst loading, and only visible light as a light source.

Under optimized conditions, HER (Fig. 5d) and 5-h time-dependent H_2 evolution profiles (Fig. 5e) of pure CdS and CQDs/CdS composites under visible-light irradiation were investigated. Pure CdS exhibited the lowest H_2 generation performance, indicating significant recombination of photogenerated charge carriers, which hinders its long-term photocatalytic efficiency. In contrast, all CQDs/CdS composites demonstrated markedly enhanced H_2 production, confirming that the incorporation of CQDs effectively promotes charge separation and prolongs carrier lifetimes. Among the tested catalysts, 12CQDs/CdS demonstrates the best performance, achieving the highest cumulative H_2 yield of 7,812.5 μmol/g over 5 h. The cumulative H_2 generation for pure CdS, 6CQDs/CdS, and 18CQDs/CdS are 4,633.5, 6,062.6, and 6,855.6 μmol/g, respectively. These results clearly highlight the critical role of CQDs in enhancing photocatalytic H_2 generation and identify 12CQDs/CdS as the optimal composition for maximum efficiency. Notably, this enhanced performance is achieved at a relatively low CQD loading, highlighting the high interfacial efficiency of CQDs in facilitating charge extraction and transport. At that optimal loading, CQDs

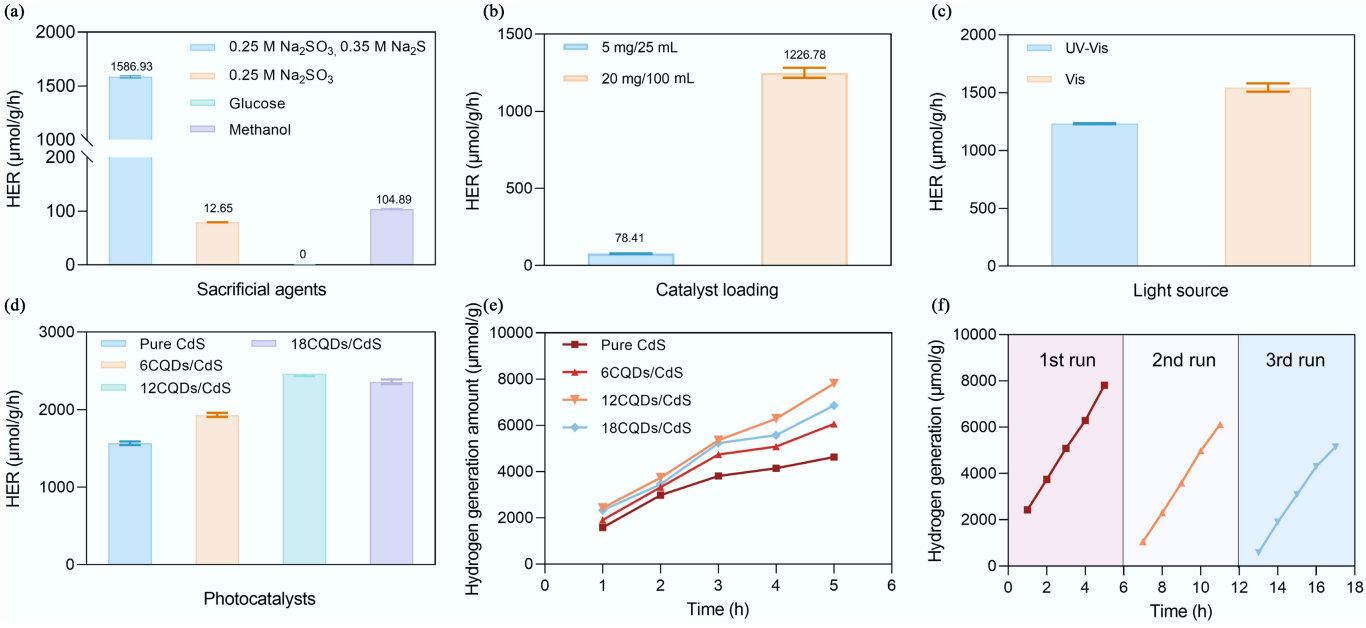

Fig. 5 (**a**) Photocatalytic H_2 evolution rate of CdS with different sacrificing agents; (**b**) HER of CdS loading at 5 mg/25 mL, and 20 mg/100 mL (UV-vis light irradiation); (**c**) HER of CdS under UV-vis and vis light irradiation (20 mg/100 mL); (**d**) HER of different CdS based catalyst; (**e**) time-dependent photocatalytic H_2 evolution profiles over 1–5 h; (**f**) photostability and reusability performance of the 12CQDs/CdS composite.

enhance the effective interfacial contact with CdS, facilitating electron extraction and interfacial charge transfer. However, with further increasing CQD content (18CQDs/CdS), their role gradually shifts from interfacial modification to excessive surface coverage, which can partially block active sites and limit the contact between CdS and reactants (e.g., H^+ and sacrificial agents), thereby suppressing surface reaction kinetics[38]. This trend is consistent with the UV-vis DRS spectra, where 18CQDs/CdS exhibits reduced effective light utilization compared to 12CQDs/CdS. Moreover, at high loading levels, CQDs may partially act as recombination centers rather than electron mediators. The aggregation of CQDs or the formation of a quasi-continuous carbon layer can lead to electron trapping in surface states, thereby increasing the probability of non-radiative recombination and reducing the overall photocatalytic efficiency[39].

To further evaluate the performance of the CQDs/CdS system, Supplementary Table S1 summarizes the comparative results with representative CdS-based photocatalysts reported in recent years. It can be seen that the optimized 12CQDs/CdS composite exhibits a competitive H_2 evolution rate compared to some previously reported systems (such as C-dot@CdS [1,582 μmol/g/h] and CdS/MoS_2 [1,984 μmol/g/h]) and is comparable to or higher than many heterostructured and co-catalyst-modified CdS systems.

Furthermore, the reusability of CdS-based catalysts was further assessed over three consecutive photocatalytic cycles (Fig. 5f). A gradual decrease in H_2 generation was observed in the second and third runs, likely due to the photocorrosion of CdS during extended light exposure[9]. The decline emphasizes the limited long-term stability of CdS-based photocatalysts under repeated photocatalytic processes.

Mechanism of photocatalytic process

To elucidate the photocatalytic mechanism of H_2 generation over CQDs/CdS composites, photoelectrochemical measurements and photoluminescence (PL) analysis were performed on the solid photocatalysts. Figure 6a exhibits the Mott-Schottky plots of pure CdS recorded at three different frequencies (500, 750, and 1,000 Hz). The positive slopes of the plots confirm that CdS is an n-type semiconductor. The flat-band potential (E_{fb}) was determined from the intercept of the linear region in the Mott-Schottky plots, derived from the relationship between $1/C^2$ and E, where C represents the space-charge capacitance of CdS. As shown in Fig. 6a, all three frequencies yield similar E_{fb} values of –0.75 V (vs Ag/AgCl), equivalent to –0.55 V (vs NHE).

$$E_{vs\ NHE} = E_{vs\ Ref} + E^0_{Ref\ vs\ NHE} \quad (3)$$

where, NHE and Ref are normal H_2 electrode, and standard potential electrode; E_{vsNHE}, $E_{vs\ Ref}$, and $E^0_{Ref\ vs\ NHE}$ are electrode potential converted to the NHE, experimentally measured electrode potential referenced to the standard potential, and standard potential electrode difference between the Ref and NHE; $E^0_{Refvs\ NHE}(1\ M\ KCl\ Ag/AgCl) = 0.197\ V$.

For n-type semiconductors, the Fermi level (Ef) lies close to the flat-band potential, which approximates the conduction band minimum, (CBM). This potential is more negative than the redox potential of water (0 V vs NHE), indicating that CdS possesses sufficient thermodynamic driving force for photocatalytic H_2 evolution. In this system, the introduction of CQDs does not significantly alter the band positions of CdS, but rather enhances charge separation and interfacial electron transfer. According to the Tacu plot-derived bandgap energy of CdS (≈ 2.05 eV) and 12CQDs/CdS (≈ 2.01 eV), the valence band maximum (VBM) was calculated to be around 1.50 and 1.46 V, respectively, further confirming its suitability for photocatalytic H_2 reaction.

The data from transient photocurrent measurements were recorded to investigate the charge separation efficiency of the materials. As shown in Fig. 6b, the chronoamperometric (i-t) curves of pure CdS and CQDs/CdS composites with varying CQD loading display periodic light on/off cycles. The 12CQDs/CdS composites exhibit the highest average photocurrent density of 49.9 μA/cm^2 at 0.4 V potential, which is nearly 20 times greater than that of pure CdS (2.63 μA/cm^2). This significant enhancement indicates that the

https://doi.org/10.48130/scm-0026-0020

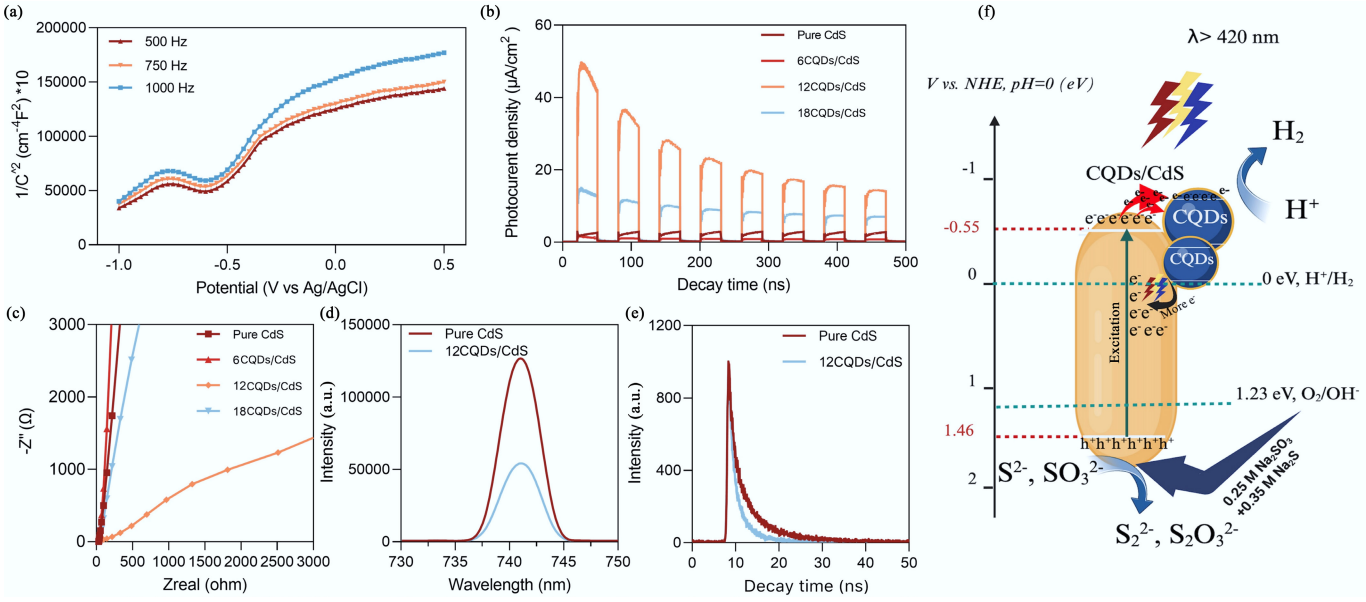

Fig. 6 (**a**) Mott-Schottky of pure CdS; (**b**) transient photocurrent response; (**c**) Nyquist plot; (**d**) steady-state photoluminescence (PL); (**e**) time-resolved photoluminescence (TRPL) spectra; (**f**) schematic representation of the photocatalytic H_2 evolution mechanism of CQDs/CdS composite.

incorporation of CQDs effectively promotes charge separation and suppresses electron-hole recombination in the CQD/CdS composites. However, a gradual decrease in photocurrent density with continuous irradiation was observed for most CQDs/CdS composites, suggesting partial photocorrosion of CdS during prolonged irradiation. This trend is consistent with the photocatalytic stability and reusability performance of H_2 generation observed for the 12CQDs/CdS catalyst. Additionally, Nyquist plots (Fig. 6c) were further employed to investigate the interfacial charge transfer behavior of CdS and CQDs/CdS composites. In the Nyquist plots, the semicircular arc represents radius charge transfer resistance, where a smaller radius corresponds to lower resistance and better conductivity. An equivalent circuit model was employed to quantitatively analyze the electrochemical impedance spectroscopy (EIS) data. The Nyquist plots were fitted based on this model (Supplementary Fig. S3), and the extracted parameters, including Rs, Rct, and CPE, are summarized in Supplementary Table S2. Notably, the Rct value decreases from 17.81 kΩ for pure CdS to 12.65 kΩ for 12CQDs/CdS, indicating facilitated interfacial charge transfer upon CQDs incorporation. Among all the catalysts, the 12CQDs/CdS composite exhibits the smallest semicircle radius, indicating that it has superior charge transport and interfacial conductivity compared to pure CdS. The enhanced electron mobility across the CQDs/CdS interface contributes directly to the improved photocatalytic H_2 evolution efficiency.

To further understand the photocatalytic mechanism of H_2 generation, the charge carrier separation efficiency of pure CdS and CQDs/CdS composites was estimated using steady-state PL spectroscopy (Fig. 6d). Upon excitation at 370 nm, both pure CdS and the CQDs/CdS composite exhibited an emission peak around 741 nm. The markedly lower PL intensity observed for the 12CQDs/CdS composite compared to pure CdS indicates a reduced recombination rate of photogenerated electron-hole pairs and more efficient charge separation. Figure 6e presents the time-resolved fluorescence decay profiles of pure CdS and 12CQDs/CdS. The 12CQDs/CdS exhibits slower fluorescence decay, suggesting a longer carrier lifetime, which is consistent with the steady-state PL results, confirming that the introduction of CQDs effectively enhances charge separation and suppresses recombination in CdS, thereby contributing to improved photocatalytic performance.

Based on the comprehensive characterization results, a tentative mechanism for photocatalytic H_2 evolution over CQDs/CdS composites is proposed in Fig. 6f. Under visible-light irradiation, CdS absorbs photons and generates electron-hole pairs, where electrons are excited from the valence band (VB) to the conduction band (CB), leaving holes in the VB. The presence of 0.25 M Na_2SO_3 and 0.35 M Na_2S as sacrificial agents consumes these photogenerated holes, thereby minimizing charge recombination. Due to their excellent electrical conductivity, the CQDs act as efficient electron acceptors, capturing photoexcited electrons from CdS and facilitating their rapid transfer. This process further suppresses electron-hole recombination. In addition, CQDs also serve as photosensitizers, broadening the light absorption range and promoting the generation of additional charge carriers. Overall, the synergistic effects of CQDs, functioning both as photosensitizers and electron mediators, significantly enhance charge separation and interfacial charge transport, resulting in superior photocatalytic H_2 production efficiency.

Conclusions

In this study, cellulose-derived carbon quantum dots (CQDs) were successfully synthesized via a hydrothermal process and integrated with CdS nanoparticles to enhance photocatalytic hydrogen (H_2) production under visible-light irradiation. Comprehensive characterization confirmed that the CQDs were uniformly anchored onto the CdS surface, resulting in improved visible-light absorption, higher electrical conductivity, reduced bandgap energy, and more efficient charge carrier separation. Photocatalytic H_2 generation evaluations demonstrate that the incorporation of CQDs significantly enhances H_2 evolution performance compared to pristine CdS. The best performance was observed for the 12CQDs/CdS composite, achieving a maximum H_2 yield of 7,812.429 μmol/g over 5 h, nearly twice that of pristine CdS.

This enhancement is primarily attributed to the dual functionality of CQDs, acting as photosensitizers to expand the light absorption and as electron acceptors to facilitate charge transfer while minimizing recombination losses. Although the CQDs/CdS composites demonstrated improved activity, a gradual decline in performance during reusability tests indicated that CdS photocorrosion remains a limiting factor, necessitating further optimization and modification strategies to enhance durability. In addition, while the interfacial role of CQDs has been demonstrated, further in-depth investigations (e.g., advanced spectroscopic analysis or theoretical calculations) are required to fully elucidate the charge-transfer mechanism.

Future work could focus on enhancing the structural stability of CdS-based systems, for example, through protective layer design, cocatalyst optimization, or heterostructure engineering, as well as further tuning the surface chemistry of CQDs to improve charge separation efficiency.

Supplementary information

It accompanies this paper at: https://doi.org/10.48130/scm-0026-0020.

Author contributions

The authors confirm their contributions to the paper as follows: Zijing Wang: data curation, investigation, formal analysis, visualization, writing – original draft. Rahil Changotra: conceptualization, writing – review and editing. Guofa Dong: resources; Jie Yang: writing – review and editing, supervision. Quan Sophia He: funding, supervision, writing – review and editing. All authors reviewed the results and approved the final version of the manuscript.

Data availability

All data generated or analyzed during this study are included in this published article and its supplementary information files.

Acknowledgments

The authors also acknowledge the A. David Crowe Graduate Scholarship for supporting this research.

Funding

The authors are grateful for the financial support from the Discovery Grant, National Science and Engineering Research Council (NSERC), Canada, awarded to Dr. Quan Sophia He (Grant No. RGPIN-2026-06983).

Declarations

Competing interests

The authors declare that they have no conflict of interest.

Author details

[1]Department of Engineering, Faculty of Agriculture, Dalhousie University, TruroNS, B2N 5E3, Canada; [2]Fujian Key Laboratory of Functional Marine Sensing Materials, College of Materials and Chemical Engineering, Minjiang University, Fuzhou 350108, China; [3]Institute of Oceanography, College of Geography and Oceanography, Minjiang University, Fuzhou 350108, China

References

[1] Al-Shetwi AQ. 2022. Sustainable development of renewable energy integrated power sector: trends, environmental impacts, and recent challenges. *Science of The Total Environment* 822:153645

[2] Goodarzi N, Ashrafi-Peyman Z, Khani E, Moshfegh AZ. 2023. Recent progress on semiconductor heterogeneous photocatalysts in clean energy production and environmental remediation. *Catalysts* 13:1102

[3] Ng KH, Lai SY, Cheng CK, Cheng YW, Chong CC. 2021. Photocatalytic water splitting for solving energy crisis: myth, fact or busted? *Chemical Engineering Journal* 417:128847

[4] Fujishima A, Honda K. 1972. Electrochemical photolysis of water at a semiconductor electrode. *Nature* 238:37–38

[5] Dhiman P, Rana G, Kumar A, Sharma G, Vo DN, et al. 2022. ZnO-based heterostructures as photocatalysts for hydrogen generation and depollution: a review. *Environmental Chemistry Letters* 20:1047–1081

[6] Wang G, Ling Y, Wang H, Yang X, Wang C, et al. 2012. Hydrogen-treated WO_3 nanoflakes show enhanced photostability. *Energy & Environmental Science* 5:6180–6187

[7] Yuan YJ, Chen D, Yu ZT, Zou ZG. 2018. Cadmium sulfide-based nanomaterials for photocatalytic hydrogen production. *Journal of Materials Chemistry A* 6:11606–11630

[8] Yang S, Guan H, Zhong Y, Quan J, Luo N, et al. 2021. CdS@Ni3S2 for efficient and stable photo-assisted electrochemical (P-EC) overall water splitting. *Chemical Engineering Journal* 405:126231

[9] Nasir JA, Rehman ZU, Ali Shah SN, Khan A, Butler IS, et al. 2020. Recent developments and perspectives in CdS-based photocatalysts for water splitting. *Journal of Materials Chemistry A* 8:20752–20780

[10] Mandal S, Adhikari S, Murmu M, Kim BH, Kim DH. 2025. Graphene and carbon quantum dots: competing carbons in harmonized photoelectrochemical platforms. *Small* 21:e05846

[11] Tian J, Leng Y, Zhao Z, Xia Y, Sang Y, et al. 2015. Carbon quantum dots/hydrogenated TiO_2 nanobelt heterostructures and their broad-spectrum photocatalytic properties under UV, visible, and near-infrared irradiation. *Nano Energy* 11:419–427

[12] Backes CW, Reis FB, Strapasson GB, Assis M, Longo E, et al. 2025. Green synthesis of carbon quantum dots for enhancing photocatalytic activity: hydrogen/oxygen evolution and dye photodegradation. *Catalysis Today* 443:114996

[13] Qin J, Zeng H. 2017. Photocatalysts fabricated by depositing plasmonic Ag nanoparticles on carbon quantum dots/graphitic carbon nitride for broad spectrum photocatalytic hydrogen generation. *Applied Catalysis B: Environmental* 209:161–173

[14] Smrithi SP, Kottam N, Vergis BR. 2022. Heteroatom modified hybrid carbon quantum dots derived from *Cucurbita pepo* for the visible light driven photocatalytic dye degradation. *Topics in Catalysis* 68:1427–1438

[15] Kiriyanthan RM, Radha A, Maharajan T, Chellasamy G. 2023. Carbon quantum dots biosynthesis: perspectives and challenges. in *Carbon and Graphene Quantum Dots for Biomedical Applications*, eds Yun K, Govindaraju S. US: Woodhead Publishing. pp. 9–22 doi: 10.1016/B978-0-323-98362-4.00011-8

[16] Kang C, Huang Y, Yang H, Yan XF, Chen ZP. 2020. A review of carbon dots produced from biomass wastes. *Nanomaterials* 10:2316

[17] Wang Z, Changotra R, Dasog M, Singh Selopal G, Yang J, et al. 2025. Carbon quantum dots: synthesis *via* hydrothermal processing, doping strategies, integration with photocatalysts, and their application in photocatalytic hydrogen production. *Sustainable Materials and Technologies* 44:e01386

[18] Eastman JW. 1967. Quantitative spectrofluorimetry-the fluorescence quantum yield of quinine sulfate. *Photochemistry and Photobiology* 6:55–72

[19] Guan X, Li Z, Geng X, Lei Z, Karakoti A, et al. 2023. Emerging trends of carbon-based quantum dots: nanoarchitectonics and applications. *Small* 19:2207181

[20] Chai YY, Qu DP, Ma DK, Chen W, Huang S. 2018. Carbon quantum dots/Zn^{2+} ions doped-CdS nanowires with enhanced photocatalytic

activity for reduction of 4-nitroaniline to p-phenylenediamine. *Applied Surface Science* 450:1–8
[21] Gogoi D, Koyani R, Golder AK, Peela NR. 2020. Enhanced photocatalytic hydrogen evolution using green carbon quantum dots modified 1-D CdS nanowires under visible light irradiation. *Solar Energy* 208:966–977
[22] Solanki RG, Rajaram P, Bajpai PK. 2018. Growth, characterization and estimation of lattice strain and size in CdS nanoparticles: X-ray peak profile analysis. *Indian Journal of Physics* 92:595–603
[23] Sami M, El-Khouly ME, Ghali M. 2024. Solvent mediated synthesis of multicolor narrow bandwidth emissive carbon quantum dots and their potential in white light emitting diodes. *Scientific Reports* 14:24812
[24] Rajamanikandan S, Biruntha M, Ramalingam G. 2022. Blue emissive carbon quantum dots (CQDs) from bio-waste peels and its antioxidant activity. *Journal of Cluster Science* 33:1045–1053
[25] Guo X, Qing Y, Wu Y, Wu Q. 2016. Molecular association of adsorbed water with lignocellulosic materials examined by micro-FTIR spectroscopy. *International Journal of Biological Macromolecules* 83:117–125
[26] Wang N, Lin J, Li Y, Li T, Chen Y, et al. 2024. One-pot synthesis of high performance CQDs/TiO_2 nanocomposites without carbon source addition. *Journal of Water Process Engineering* 65:105833
[27] Shurvell HF. 2006. Spectra– structure correlations in the mid- and far-infrared. In *Handbook of Vibrational Spectroscopy*, eds Chalmers JM, Griffiths PR. US: John Wiley & Sons, Ltd. doi: 10.1002/0470027320.s4101
[28] Rao Y, Inwati GK, Singh M. 2021. Green synthesis, structural characterization and application of cadmium sulfide nanocrystals with fluorescent dyes for solar enhancement. *Advanced Materials Proceedings* 2:223–227
[29] Fadley CS, Shirley DA. 1970. Electronic densities of states from X-ray photoelectron spectroscopy. *Journal of Research of the National Bureau of Standards Section A: Physics and Chemistry* 74A:543–558
[30] Mahmood A, Shi G, Wang Z, Rao Z, Xiao W, et al. 2021. Carbon quantum dots-TiO_2 nanocomposite as an efficient photocatalyst for the photodegradation of aromatic ring-containing mixed VOCs: an experimental and DFT studies of adsorption and electronic structure of the interface. *Journal of Hazardous Materials* 401:123402
[31] Yu J, Yu Y, Zhou P, Xiao W, Cheng B. 2014. Morphology-dependent photocatalytic H_2-production activity of CdS. *Applied Catalysis B: Environmental* 156–157:184–191
[32] Dager A, Uchida T, Maekawa T, Tachibana M. 2019. Synthesis and characterization of Mono-disperse Carbon Quantum Dots from Fennel Seeds: photoluminescence analysis using Machine Learning. *Scientific Reports* 9:14004
[33] Moniruzzaman M, Lakshmi BA, Kim S, Kim J. 2020. Preparation of shape-specific (trilateral and quadrilateral) carbon quantum dots towards multiple color emission. *Nanoscale* 12:11947–11959
[34] Xue J, Fujitsuka M, Majima T. 2019. Shallow trap state-induced efficient electron transfer at the interface of heterojunction photocatalysts: the crucial role of vacancy defects. *ACS Applied Materials & Interfaces* 11:40860–40867
[35] Raghavan A, Sarkar S, Nagappagari LR, Bojja S, MuthukondaVenkatakrishnan S, et al. 2020. Decoration of graphene quantum dots on TiO_2 nanostructures: photosensitizer and cocatalyst role for enhanced hydrogen generation. *Industrial & Engineering Chemistry Research* 59:13060–13068
[36] Chen Y, Zhong W, Chen F, Wang P, Fan J, et al. 2022. Photoinduced self-stability mechanism of CdS photocatalyst: the dependence of photocorrosion and H_2-evolution performance. *Journal of Materials Science & Technology* 121:19–27
[37] Meinhardová V, Dubnová L, Drobná H, Matějová L, Kočí K, et al. 2023. Role of lamp type in conventional batch and micro-photoreactor for photocatalytic hydrogen production. *Frontiers in Chemistry* 11:1271410
[38] Mou Z, Wu Y, Sun J, Yang P, Du Y, et al. 2014. TiO_2 nanoparticles-functionalized N-doped graphene with superior interfacial contact and enhanced charge separation for photocatalytic hydrogen generation. *ACS Applied Materials & Interfaces* 6:13798–13806
[39] Ghosh S, Sarkar D, Bastia S, Chaudhary YS. 2023. Band-structure tunability *via* the modulation of excitons in semiconductor nanostructures: manifestation in photocatalytic fuel generation. *Nanoscale* 15:10939–10974

Copyright: © 2026 by the author(s). Published by Maximum Academic Press, Fayetteville, GA. This article is an open access article distributed under Creative Commons Attribution License (CC BY 4.0), visit https://creativecommons.org/licenses/by/4.0/.